Corrosion mechanism of a Ni-based alloy in supercritical water: Impact of surface plastic deformation

Mickaël Payet[a,b], Loïc Marchetti[b,*], Michel Tabarant[c], Jean-Pierre Chevalier[a,d]

[a] Conservatoire National des Arts et Métiers, Matériaux Industriels, 292 rue Saint-Martin, 75141 Paris cedex 3, France
[b] CEA, DEN, DPC, SCCME, Laboratoire d'Étude de la Corrosion Aqueuse, F-91191 Gif-Sur-Yvette Cedex, France
[c] CEA, DEN, DPC, SEARS, Laboratoire d'Ingénierie des Surfaces et Lasers, F-91191 Gif-Sur-Yvette Cedex, France
[d] PIMM, UMR 8006 Arts et Métiers ParisTech/Cnam/CNRS, 151 Bd de l'Hôpital, 75013 Paris, France

A B S T R A C T

Ni–Fe–Cr alloys are expected to be a candidate material for the generation IV nuclear reactors that use supercritical water at temperatures up to 600 °C and pressures of 25 MPa. The corrosion resistance of Alloy 690 in these extreme conditions was studied considering the surface finish of the alloy. The oxide scale could suffer from dissolution or from internal oxidation. The presence of a work-hardened zone reveals the competition between the selective oxidation of chromium with respect to the oxidation of nickel and iron. Finally, corrosion mechanisms for Ni based alloys are proposed considering the effects of plastically deformed surfaces and the dissolution.

Keywords:
A. Nickel alloy
C. High temperature corrosion
C. Intergranular corrosion
C. Internal oxidation
C. Selective oxidation

1. Introduction

Interest in supercritical water (SCW) is growing both for organic waste decomposition and for energy production [1,2]. The use of SCW for the supercritical water-cooled reactor (SCWR), one of the Generation IV nuclear reactor concepts, is of particular interest due to the relationship between steam temperature and boiler efficiency. The SCWR is an evolution of the light water reactors presently in service. The present design concept for the SCWR requires the materials to withstand a core coolant temperature of between 280 °C and 620 °C at a pressure of 25 MPa. In such conditions, the selection of corrosion resistant materials is one of the key issues for the development of the SCWR concept [3,4]. One of the critical issue remains with the selection of the fuel cladding material, where the material must withstand the greatest temperature and pressure conditions. Consequently, studies on the corrosion properties of metallic alloys at the extreme conditions at 600 °C and 25 MPa are of significant importance for the SCWR concept.

Several studies on the corrosion of Fe–Ni–Cr alloys have been carried out for the SCWR concept. These have focused on the following aspects: the effect of the test water's chemical composition [6–8], the alloy's chemical composition [9–11], the effect of surface finish [12], the alloy's microstructure [5,9,10], and the effect of stress for studying the alloy's stress corrosion cracking resistance [13,14].

The characterization of the corrosion properties of nickel-based (Ni–Cr–Fe) and iron-based (Fe–Ni–Cr) alloys has largely been focused on in studies conducted for the SCWR reactor. Comparing the oxide scale that forms on nickel-based and on iron-based alloys after exposure to similar SCW conditions typically reveals a significant difference of thickness. For nickel-based alloys, the oxide layer is much thinner [8,15–17] than in the case of steels [5,13]. These observations agree with the significantly lower weight gains on nickel-based alloy samples compared to the gains for steel samples. The difference in the oxide thickness and weight gain when comparing these two alloy classes is believed to be due to the higher chromium content within studied nickel-based alloys. Indeed chromium rich oxides, such as α-chromia or mixed chromites are expected to form the protective part of the oxide on Ni–Cr–Fe alloys. These alloys thus appear more corrosion resistant.

More details on the oxide composition are necessary to propose mechanism describing the different oxide morphologies. Guzonas et al. [16] used Raman spectroscopy to describe the oxide layer composition. They performed SCW corrosion tests at 450 °C and 23 MPa during 483 h on many Fe–Ni–Cr alloys. The oxide layer typically

* Corresponding author. Present address: CEA, DEN, DTCD, SECM, Laboratoire d'étude du Comportement à Long Terme des Matériaux de conditionnement, F-30207 Bagnols-sur-Cèze, France.
E-mail address: loic.marchetti@cea.fr (L. Marchetti).

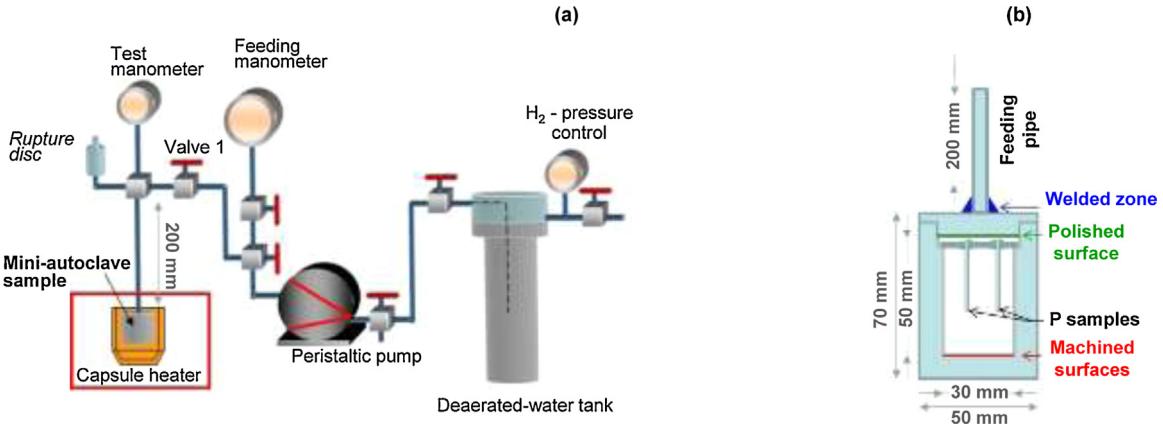

Fig. 1. (a) Scheme of the experimental set-up and (b) scheme of a mini-autoclave.

consisted of mixed spinel oxides $Ni_xFe_yCr_zO_4$ whose compositions depended on the alloy composition. They identified, especially on Alloy 690, $NiFe_2O_4$ and assumed the presence of chromia. Maslar et al. [18] similarly used Raman spectroscopy to identify the sole presence of $NiFe_2O_4$ within the oxide scale that formed on a polished (alumina gel finish) alloy 600 (Ni–15Cr–8Fe–Mn–Ti–Si) sample after testing at 543 °C and 25.4 MPa. Maslar et al. [18] also investigated the influence of surface finish on the phases present with the oxide layer. It was determined that polishing alloy 600 with a coarse grain SiC paper induced the formation of both $NiFe_2O_4$ and traces of α-chromia. In the same way, in different conditions of temperature and pressure, the oxide morphology or the corrosion kinetics [19–21] has been shown to be dependent on the surface finish of the alloy sample. In subcritical condition (325 °C and 15 MPa), *i.e.*, in simulated primary media of a pressurised water-cooled reactor (PWR), Lefaix-Jeuland et al. [20] showed that the chromia morphology was dependent on the crystallographic defect structure present near the surface of the sample prior to testing. A high content of subsurface defects leads to a high density of chromia nodules at the oxide/alloy interface. In contrast, a low defect density induces fewer chromia nodules at the same interface. Moreover, Lefaix-Jeuland et al. reported that the evolution of oxidation kinetics exhibited by these two types of samples (high and low defect densities) differed strongly. Here, the corrosion behavior of Ni base alloys in supercritical water has been studied taking into account the alloy surface finish.

The physical state of the corrosion medium must also be taken into account when studying corrosion of nickel-based and iron based alloys in SCW conditions. Dissolution is specific of corrosion in a liquid phase, whereas, volatile compounds can be formed within gaseous environment. At 600 °C and 25 MPa, supercritical water is expected to have a behavior close to the vapor phase, according to its physical properties [22,23]. Nevertheless, Guzonas and al. [16] mentioned some dissolution in supercritical conditions at 500 °C and 25 MPa corresponding to a liquid behavior, whereas, a vapor behavior could also be expected.

In this present work, the generalized corrosion of the Ni-based Alloy 690 was studied in SCW conditions at 600 °C and 25 MPa. As these temperature is not sufficient to produce volatile compounds of chromium, particular attention was focused on the possibility of some dissolution in SCW. Moreover, these results compare a polished reference state to a machined surface (as described below) in order to investigate the corrosion behavior of nickel-based alloys in SCW as a function of the alloy's surface finish. The corrosion mechanisms taking both the dissolution and the effect of the surface finish into account have been discussed based on these results.

2. Material and methods

2.1. Corrosion test experiments

The present study focuses on corrosion in extreme SCW conditions, *i.e.*, at 600 °C and 25 MPa, supposing that an alloy in these conditions would exhibit equal or greater resistance at less exacting conditions.

At 600 °C and 25 MPa, SCW is expected to behave similar to the vapor phase according to its physical properties (see Section 1). However, regarding the published data [16], some metal dissolution may occur in these conditions that could cause contamination of the test samples from the dissolution of the testing apparatus materials.

Consequently, a specific corrosion device had to be used in order to avoid any possible pollution of the test samples. This methodology also allows for accurate conclusions to be made about the alloy test sample's dissolution in SCW conditions. For these purposes and also to avoid any coupling effects during the corrosion test, this study used mini-autoclaves and coupons that were made of the same alloy. Thus, both the coupons and the mini-autoclaves were used as test samples. The mini-autoclave (Fig. 1) was a cylinder with a height of approximately 5 cm and a diameter of approximately 3 cm resulting in a working volume of 35 cm^3. This corresponds to 2.5 mL of water in normal conditions of temperature and pressure.

The experimental set-up is presented in Fig. 1. It is composed of a high temperature part (a furnace containing the mini-autoclaves) and an ambient temperature part which allows the control and the adjustment of the pressure in the autoclaves. After evacuating the mini-autoclave until a primary vacuum was reached, it was introduced into the furnace at the test temperature. Feed water was introduced into the mini-autoclave from a tank with a peristaltic pump which permitted to reach the testing pressure. Afterwhich, the mini-autoclave was sealed for the duration of the test (Valve 1, Fig. 1).

The feed water consisted of ultrapure water (18.2 MΩ cm), deaerated by H_2 bubbling and maintained under a H_2 pressure of about 0.2–0.4 MPa in the tank. In these conditions, using Henry's law, the dissolved H_2 concentration does not exceed 10^{-3} molar ratio on H_2O used in the test. All corrosion tests were performed at 600 °C and 25 MPa, for three exposure times: 335 h, 840 h, and 1740 h.

2.2. Materials

Although the Alloy 690 does not have sufficient creep properties to be considered as a fuel cladding material for the SCWR,

Table 1
Composition of the alloy 690 studied.

Elements	Ni	Cr	Fe	C	Co	Mn	Al	Ti	Cu	Si	S	*P*
Composition (%w)	59.31	29.20	9.94	0.018	0.014	0.31	0.13	0.27	<0.002	0.27	<0.0005	0.007

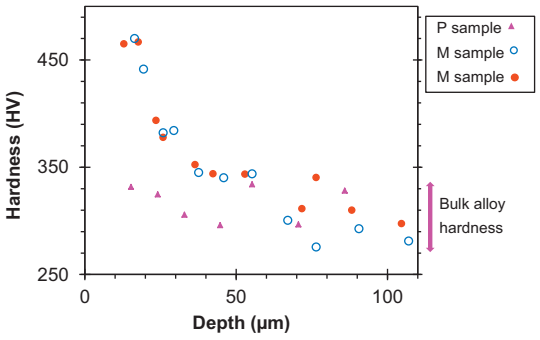

Fig. 2. Hardness profiles from *P* and *M* samples measured on cross section before corrosion test (for each measurement the standard deviation is approximately 10%).

the background concerning the corrosion behavior of this alloy (widely used in nuclear industry) in high temperature aqueous media [24] led to the choice of this alloy as an initial model system. The composition of the alloy studied is presented in Table 1. The microstructure of the alloy had a equiaxed grains of around 20–30 μm, with $M_{23}C_6$ intergranular carbides (where M is mainly chromium) approximately 0.2 μm in size and intragranular Ti(C,N) carbides approximately 5–10 μm in size. This alloy is essentially a disordered f.c.c. solid solution.

$20 \times 30 \times 1\ mm^3$ samples were cut out from the initial sheet alloy. Two samples were suspended in each mini-autoclave. One was used for the characterizations of the oxide layer and the second one for the study of the oxide growth mechanism. The mini-autoclaves were machined from the same alloy heat. Finally the mini-autoclaves were sealed by welding only on their external faces. The Heat Affected Zone did not affect the internal face of the autoclave, which was exposed to SCW conditions.

In order to decrease the effects of a damaged sub-surface on the test sample's corrosion properties (characterized by cold working and/or roughness), the test samples are typically polished. Here, each sample was wet ground (SiC papers from grade 600–2400) and polished using 3 and 1 μm-diamond pastes and finally with 0.04 μm alumina gel. Due to the geometry of a mini-autoclaves, the internal surfaces of a mini-autoclave body could not be polished. Hence only the top flat part of each mini-autoclave has been polished in the same conditions. Thus, two kinds of surface finishes, polished and as-machined, were exposed during the corrosion tests and were subsequently studied. The polished surfaces are noted as *P* and the machined ones as *M* (Fig. 2).

As the autoclaves were machined, *M* surfaces undergo severe plastic deformation. To characterize the difference between *M* and *P* surfaces, Vickers hardness profiles were obtained using microindentation with a *CSM Instruments* instrumented indenter. The measurements were performed on cross sections, applying care to minimize any effects due to cutting and polishing.

Fig. 2 shows hardness profiles measured on the two kind of surfaces (*P* and *M*). The top surface corresponds to 0 μm depth. Due to the size of the indentations, no measurement can be made between the surface and a depth of about 10 μm. The bulk hardness of the Alloy 690 samples range between 275HV and 375HV. For the *P* samples, the measured near surface hardness shows a virtually flat profile and clearly does not exceed the bulk value. On the contrary, the hardness profile of the *M* sample decreases from 450HV at 20 μm of depth to 275HV in the bulk, which is characteristic of high density of dislocations in the vicinity of the sample surface.

Furthermore, one coupon per mini-autoclave received a specific treatment in order to study the oxide growth mechanisms. Gold inert markers were deposited on the *P* surface by sputtering. To be sure that the markers did not influence the oxidation kinetics, the following points were checked. On the sample surfaces, the markers formed widely spread clusters below 5 nm of diameter which was much smaller than the oxide layer thickness observed in this study. The markers did not affect significantly the sample roughness. The comparison (not shown here) between *P* samples with or without markers after the corrosion tests confirmed the inert character of gold in supercritical conditions. Every characterization concerning composition, morphology, or structure were similar in the two cases for the same oxidation time.

2.3. Characterizations of the oxide scale and media analyses

After a corrosion test, the mini-autoclaves were removed from the furnace and cooled to ambient temperature for 1 h. The aqueous media was removed from the mini-autoclave by a pressurized helium injection. This media was captured and subsequently analyzed by inductive-coupled-plasma optical emission spectrometry (ICP-OES), using a *PerkinElmer Optima 2000*.

In order to carry out a detailed analysis of the oxide scale structures formed, several characterization techniques were used. The morphology of the oxide layer was studied, using both surface and cross-sectional views, by field-emission gun scanning electron microscopy (FEG-SEM *Zeiss* ultra 55). Some cross sections were prepared after sputtering silver on the samples after the corrosion test in order to be sure that the preparation procedure does not alter the oxide layer. The oxide chemical composition was characterized using energy dispersive spectroscopy (EDS) coupled in the SEM and also by glow discharge optical spectrometry (GDOS), using a *GD-Profiler* from *Horiba-Jobin Yvon*. The crystallographic structures of the oxides were analyzed by X-ray diffraction (XRD) using a *X'Pert MPD from Panalytical*.

3. Results

3.1. Evolution of the oxide scale: polished (P) samples

The oxide layers that formed on polished surfaces changed significantly with the exposure time in hydrogenated SCW conditions and results are presented comparing the two extreme exposure times: 335 h and 1740 h. For the samples exposed for 840 h, the structure of the oxide scale was quite similar to that of the samples exposed for 1740 h.

Surface observations by SEM (Fig. 3) show an inhomogeneous surface, with two kinds of zones whatever the exposure time. The large zones (bright contrast on Fig. 3c) contained larger oxide crystallites that were about 1–3 μm in size (Fig. 3a–d). The size of the large zone is about 30 μm which is similar to the alloy grain size.The major difference between the samples oxidized for 335 h and 1740 h is the density of the oxide crystallites; this decreased with the oxidation time (Fig. 3c and d). It is of note that the shape of the oxide crystallites was better defined (sharper edges) after 335 h of exposure than after 1740 h of exposure (Fig. 3a and b). It can be proposed that this evolution of shape when increasing the exposition time is a consequence of the dissolution. The second kind of

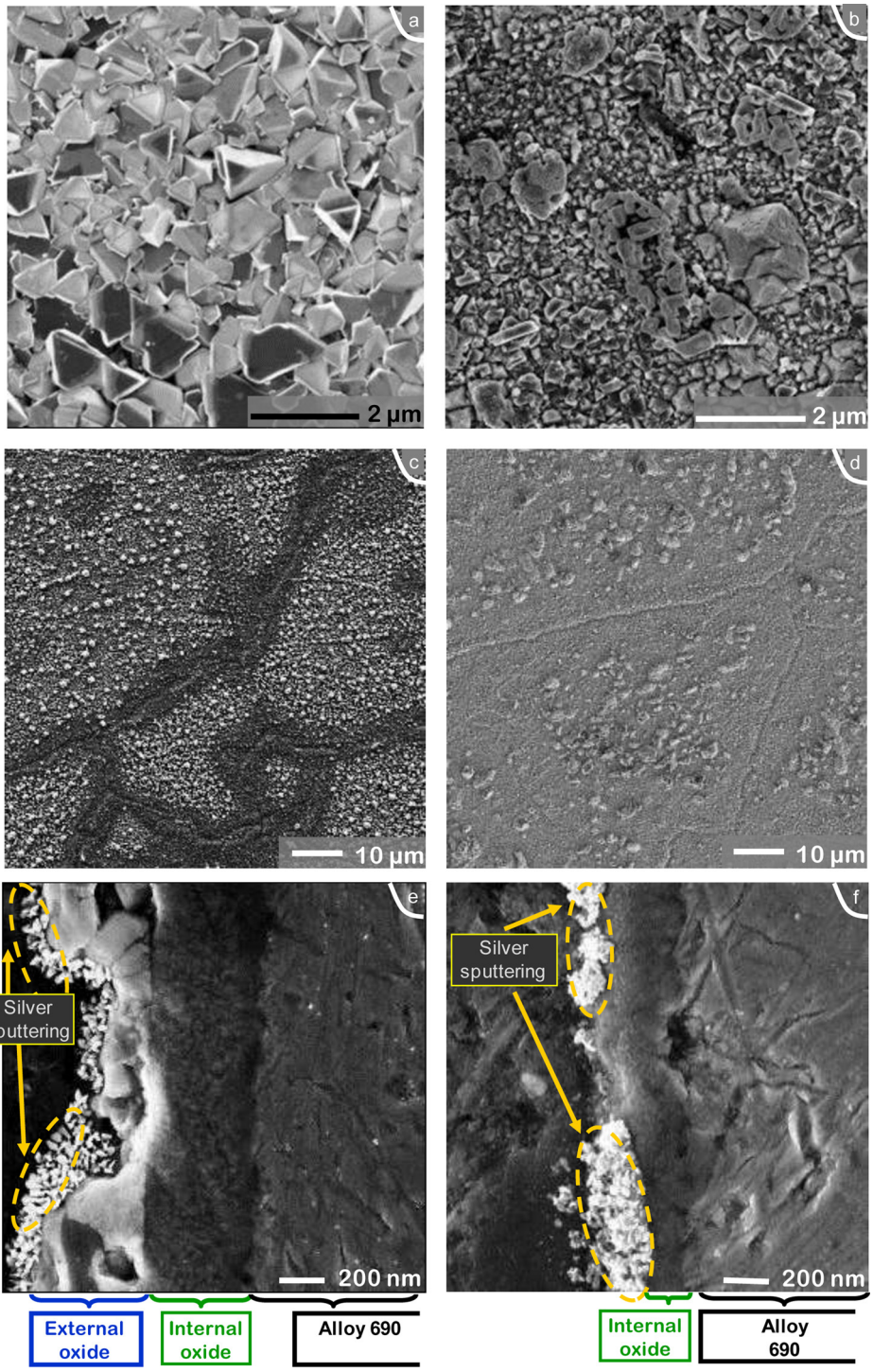

Fig. 3. SEM observations [mainly performed at 5 kV] of Alloy 690 *P* samples exposed in hydrogenated SCW. (a) Surface [at 3 kV], (c) surface [at 10 kV], and (e) cross-section views of 335 h-oxidized sample. (b), (d) Surface and (f) cross-section views of 1740 h-oxidized sample.

zone is narrower (dark contrast on the Fig. 3c) and composed of the smallest oxide grains (below 200 nm in size). The narrow zone (1–5 µm) is larger than the alloy grain boundary, but seems to highlight the grain boundaries. The difference between these two zones (the narrow one and the large one) is the consequence of the nature of the oxidation mechanism related to the alloy microstructure. These two zones can be considered as intragranular and intergranular oxidation zones.

The decrease of oxide layer thickness with increasing exposure time was investigated using the SEM (Fig. 3e and f). After 335 h in SCW conditions, the oxide scale that formed on the Alloy 690 was around 1 µm thick and was composed of two layers. The external layer, highlighted by the silver sputtering, displays a light contrast in Fig. 3e and has non-uniform thickness (0.2 µm and greater). This agreed with the SEM observation of the corroded surface which revealed an external scale composed of oxide grains exhibiting various sizes. On the contrary, the internal layer which appears in Fig. 3e was homogeneous in thickness (roughly 500 nm). For the sample exposed for 1740 h, the external layer has almost disappeared or appeared be less adherent (for example, on Fig. 3f, the sputtered sil-

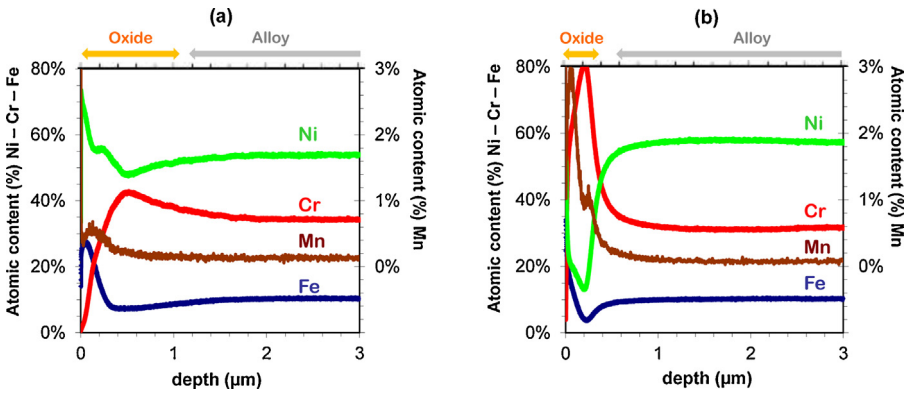

Fig. 4. Fe, Cr, Ni, and Mn GDOS atomic profiles normalized to the total metallic elements (*i.e.*, without taking oxygen into account) from *P* samples, (a) exposed 335 h in SCW and (b) exposed 1740 h.

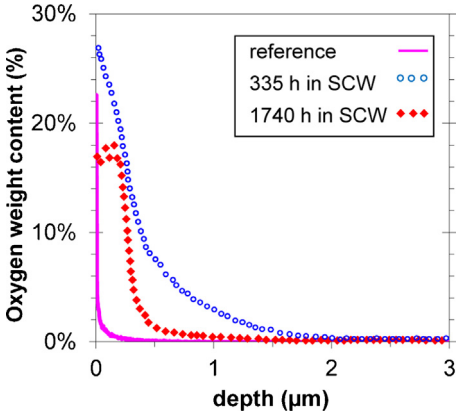

Fig. 5. O weight profiles from *P* samples, non-oxidized (reference), exposed 335 h in SCW and exposed 1740 h.

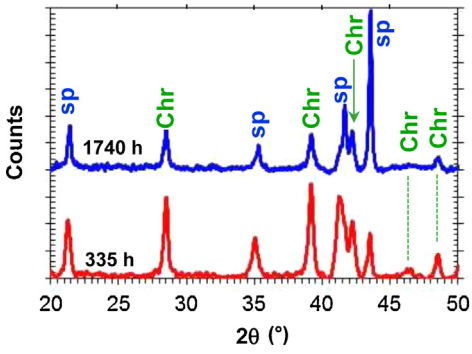

Fig. 6. XRD analysis performed in $\theta/2\theta$ of *P* samples exposed to SCW during 335 h or 1740 h (up). sp means spinel form ($M'M_2O_4$) and chr corresponds to α-chromia (Cr_2O_3).

ver remaining on the oxidized surface of the cross-sectioned sample was non-continuous (which is characteristic of the 1740 h sample). The non continuous of the silver layer suggested that oxide grains from the external layer had scaled off during the preparation of the cross-section). Only the internal oxide layer remained and its thickness is also around 500 nm. These observations confirm that the external layer disappeared when increasing oxidation time from 335 h to 1740 h.

GDOS profiles confirm that the oxide layer changed in composition with exposure time in hydrogenated SCW conditions (Figs. 4 and 5). First, as can be seen in Fig. 5, the oxygen profile was more diffuse for the 335 h-sample compared to the 1740 h-sample. This agreed with the SEM observations in cross-section, which also showed a thicker oxide layer after 335 h exposure. Secondly, in Fig. 4, relevant differences can be seen between the chromium profiles recorded on each sample. A peak chromium concentration was observed in the oxide layer regardless the exposure time but this maximum was almost doubled, from 43% after 335 h of exposure, to 80% after 1740 h.

Based on the GDOS results, the oxide scale in the 335 h sample is clearly divided into three parts marked by three successive peaks from the surface to the bulk material (one of nickel, one of manganese, and one of chromium). The external layer was enriched in nickel and iron. An intermediate layer can be defined by increased manganese content whereas, the chromium content was lower than in the bulk alloy. Finally, the internal oxide layer contained a slight enrichment of chromium while the nickel and iron content were lower compared to the bulk alloy composition.

For the 1740 h-sample, the same features exist and were more emphasized. The external layer, rich in iron and nickel, was now limited to traces on the surface. In comparison to the layer observed after shorter oxidation times, the intermediate layer, particularly enriched in manganese, was also enriched in chromium whereas, iron and nickel contents were lower. The internal oxide layer consisted of mainly chromium.

The analyses of the samples by X-ray diffraction (Fig. 6) led to the identification of two crystalline phases that have previously been published in the JCPDS data bank. Rhombohedral chromia is identified as JCPDS #01-084-1616, where the major peaks are measured at 28.5°, 39.2°, and 48.5°. The second phase appears to be a mixed spinel of the general type $M'M_2O_4$ (where M′ could be nickel, iron or manganese and M could be the preceding elements and also chromium). The major peaks for this phase occurred at 35.3°, 41.7°, and 43.7° and depended slightly on the composition of the compound. Comparing the JCPDS data of $NiCr_2O_4$ (#01-088-0108), $MnCr_2O_4$ (#00-054-0876), $NiFeCrO_4$ (#00-052-0068), and $NiFe_2O_4$ (#00-010-0325), the characteristic peaks are very close and do not allow to discriminate between these compounds. Furthermore, it is very likely that the spinels are non-stoichiometric and their compositions may change through the oxide scale thickness.

The diffractograms in Fig. 6 are presented with data normalized to the most intense peak of the f.c.c. alloy at 51.4°. This normalization suggested that the spinel proportion in the oxide layer was more greater for the 335 h-sample whereas the proportion of chromia was higher within the oxide layer of the 1740 h-sample. The elevated spinel content in the 335 h sample seems to be related to the presence of the external layer (observed by SEM) and to enrichment in iron and nickel (measured by GDOS). The increasing proportion of chromia could be linked to the disappearance of

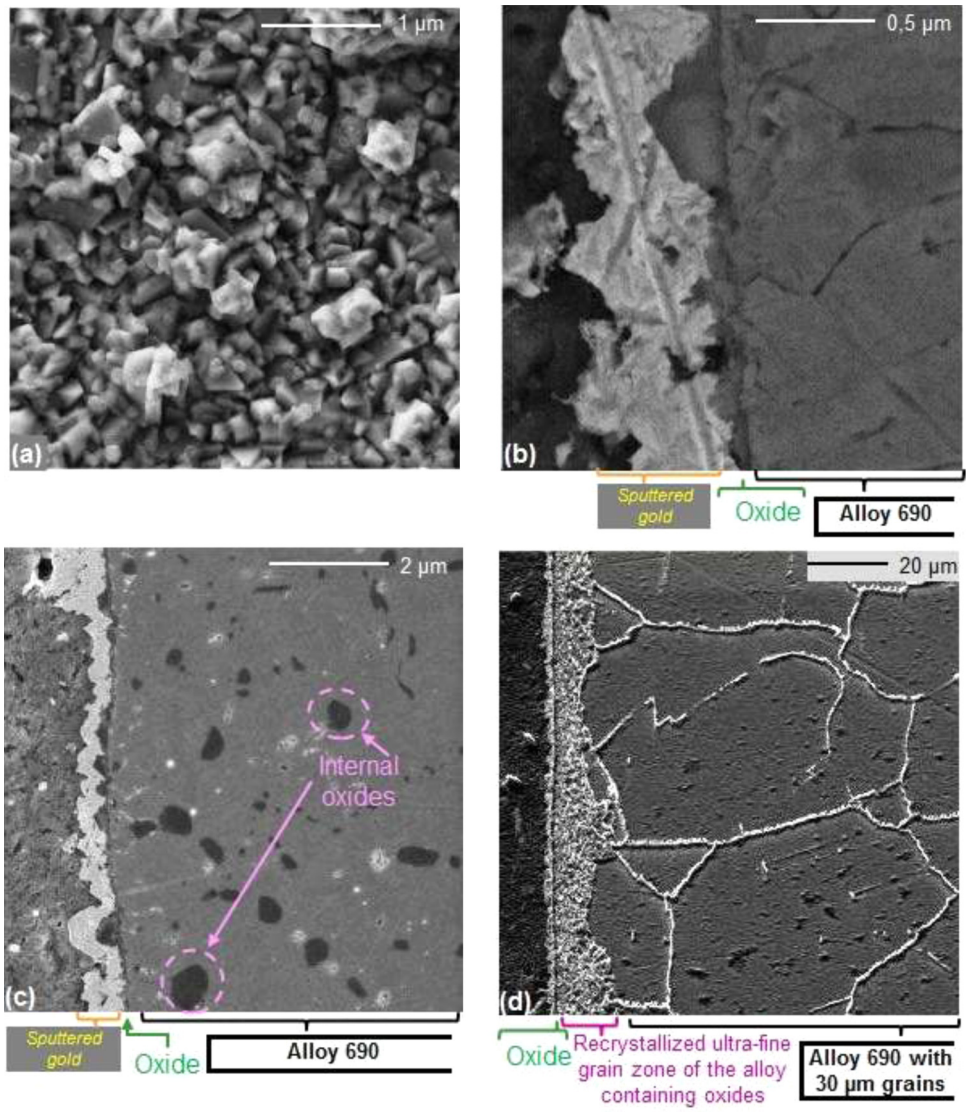

Fig. 7. SEM observations [mainly performed at 5 kV] of Alloy 690 M sample oxidized 840 h in SCW conditions (600 °C, 25 MPa). (a) Surface view showing fine crystallites and (b) cross-section observations showing the thinness of oxide layer, (c) the internal oxidation in the alloy matrix and (d) the ultra-fine grain zone induced by milling revealed by electrochemical etching [SEM acceleration voltage at 10 kV].

the external scale on 1740 h-sample and probably to an increasing content of chromia.

Due to the analysis size for GDOS or XRD (approximately 6 mm^2), these results concerned mainly the intragranular zone. This leads to the following conclusions about the structure of the oxide scale growing on polished Alloy 690 intragranular zones during exposure to hydrogenated SCW: (i) the internal scale consists of chromia; (ii) the external layer consists of mixed spinel-type oxides rich in nickel and iron and this layer tends to disappear when the sample exposure time increases from 335 h to 1740 h; (iii) between the internal and external layers, there is an intermediate layer which probably also consists of a mixed spinel. As opposed to the external layer, this scale remains when increasing exposition time and becomes richer in both Mn and Cr.

These results on the corrosion of Alloy 690 in hydrogenated supercritical water are in agreement with previous studies under SCW conditions [16,18,25]. As for the composition profiles (Fig. 5), nickel ferrite $NiFe_2O_4$ can be present in the oxide scale as reported by Guzonas et al. [16] and Maslar et al. [18]. Here, it probably corresponds to the external layer and especially to the crystallites observed on the 335 h-samples at the intragranular zone. Moreover, the morphology of the oxide layer observed in the current study after exposure for 335 h looks like the multi-layered oxide observed on nickel base Alloy in sub-critical conditions [26]. At 325 °C and 15 MPa, the oxide scale formed on the Alloy 690 is made of scattered nickel ferrite crystallites constituting the external and discontinuous layer whereas the internal and continuous one is mainly composed of iron and nickel mixed chromite, even if the presence of α-chromia nodules at the chromite/alloy interface are also reported. The characterizations carried out here reveal, on the contrary, that the internal and protective layer is mainly made of chromia, but also contains mixed chromites enriched in manganese.

3.2. *Evolution of the oxide scale: as-machined* (M) *samples*

In order to observe the difference between the polished coupons *P* and the milled-autoclave surface *M*, the flat autoclave bottom was analyzed following the same procedure. The results are compared to those from the polished surfaces. The first difference between *P* and *M* samples concerns the evolution of the oxide structure. Whatever the oxidation time, the results were similar for *M* samples

with the exception of the manganese content. For this reason, only the results for the sample exposed for 840 h are reported below.

The images obtained by SEM reveal that the oxide crystallites were much smaller for *M* surface, and were below 500 nm (compare Fig. 7a to Fig. 3a and b). In the same way, the cross sections (Fig. 7b and c) show that the oxide layer was continuous and thinner, about 200 nm thick, with large oxide crystallites (up to 500 nm pyramidal oxide crystallites lying on the oxide layer). Under the continuous scale, a dark contrast can be observed in the bulk alloy. This dark contrast is clearly observed up to a depth of 10 μm from the surface. The images were obtained in secondary electron mode. Since the surface was polished, the contrast is not topographic, but rather chemical in origin. As chemical contrast implies that contrast decreases with decreasing average atomic number, it is plausible to assume that the dark contrast are due internal oxides. EDX analyses (Fig. 8) confirmed this. The oxygen *K*-α peak at 0.52 eV was significant for the oxide layer and for the regions with dark contrast, even if the chromium *L*-α peak at 0.57 eV was close. On the contrary, intensity at 0.52 eV was low for the bulk alloy. At the same time, the chromium content increased around the regions with dark contrast. Furthermore, this was not linked to carbides since the carbon *K*-α peak at 0.27 eV was of low uniform intensity (typical of carbon pollution of the sample). Moreover the low intensity at 0.85 eV (characteristic of the nickel *L*-α peak) for the oxide and the internal oxide compared to the high level from the reference (bulk alloy) spectrum suggests that nickel was in low concentration in both the oxide and in the internal oxide. Finally, it can be suggested that the internal oxide was essentially chromium oxide.

Furthermore, after electrochemical etching (at 5 V during 20 s in an orthophosphoric acid solution) the alloy microstructure beneath the oxide layer (Fig. 7d) was revealed. An ultra-fined-grain zone was clearly visible up to 10 μm depth in the alloy below the oxide layer. In this area, the alloy grain size was below 1 μm whereas, it reached 30 μm in the bulk. This zone was not present in the *P* surface. This is probably due to the work-hardened zone formed during the milling, whereas, the polishing method used on *P* samples removes this work-hardened zone as shown by the hardness profile (Fig. 2). The sub-micron grains were formed during either the milling or, more probably, during the corrosion test by recrystallization at 600 °C. In any case, this recrystallized zone played a major role in the difference of the *P* and *M* oxide morphologies.

The analysis of the continuous oxide layer by GDOS (Fig. 9a) shows similar profiles to those obtained on *P* samples oxidized 840 h (not shown here) or 1740 h (Fig. 4b). The external layer which was rich in iron and nickel, was very thin, whereas, the internal layer was composed of chromium rich oxides. In fact, the major difference, in terms of chemistry, between *M* and *P* samples consisted of the manganese enrichment in the oxide scale which increased with the oxidation time (Fig. 9b).

To summarize, the consequence of severe plastic deformation through machining leads to the following differences in the corrosion behavior of Alloy 690 in SCW. The external layer formed on *M* sample remained very thin whatever the oxidation time. The continuous internal oxide layer was also thinner than *P* samples. The oxide enrichment in manganese was much more significant for *M* samples. Internal oxidation was observed under the continuous oxide layer up to 10 μm in depth.

3.3. Cations dissolution

Previous observations (Fig. 3) suggested that the external layer disappeared with increasing exposure time in supercritical water. To evaluate this, the test water was taken from each autoclave sample and analyzed by ICP-OES. The Table 2 presents the results and reveals a significant increase in Fe, Ni, or Mn concentrations in solution with time. Cr content was only relevant in the 1740 h-test water.

With respect to the known solvation properties of SCW, the high dissolution of Fe, Ni, and Mn cations measured here is surprising, and this leads to questions on its origin. In some cases, cooling could be the origin of an overestimation of cation release, by enhancing scaling due to thermal stresses and/or oxide dissolution due to the return of SCW to the liquid state. Nevertheless, in this study, no scaling was observed and dissolution during cooling cannot explain an increase of cations concentration with exposition time.

It can then be concluded that cations release occurred during corrosion in SCW conditions, but it was difficult to clearly identify the origin of the metallic element release, from either the *P* surface or the *M* surface. The disappearance of the external layer from *P* samples when increasing exposition time suggests this type of samples provided the major contribution to release phenomena. An evaluation of the nickel concentration, assuming the total disappearance of the external layer formed on the 335 h-*P* sample, leads to an overvaluation of one or two orders of magnitude with respect to the concentrations measured by ICP-OES. However, this overestimate could correspond to a limit in nickel solubility which would induce a precipitation on the whole surface (*P* and *M*). This hypothesis could explain the observation of scattered big crystallites on *M* samples.

3.4. Oxide scale growth mechanisms

For the study of the growth mechanisms, gold nodules (initially less than 5 nm large) were sputtered on the *P* surface and used as inert markers (see Subsection 2.2).

For each corrosion test time, gold markers were observed on the marked *P* sample surface. First, marker size grew from 5 nm to 80 nm after the supercritical condition exposure (Fig. 10b). Secondly, the marker distribution followed the oxide layer morphology (Fig. 10a). For the 335 h *P* sample, the differences between the two previous oxidation zones (*i.e.*, intergranular and intragranular define in Subsection 3.1) were emphasized. In that case, the markers were only present on the intergranular oxidation zone and are not observed on the intragranular oxidation zone (Fig. 10b).

It can be deduced that gold markers were probably hidden by the oxide layer formed on intragranular zone. These results indicate that, at least for the external layer, a cationic growth occurred on the intragranular oxidation zone whereas, an anionic growth promoted the oxide formation on the intergranular zone.

After exposure for 840 h and 1740 h, the markers were uniformly observed on the oxidized surface (not shown here), exhibiting mainly an anionic growth on the whole surface of *P* samples. Gold markers previously hidden under the cationic oxide layer were probably revealed after the dissolution of the latter. From Fig. 3e, it is more likely that above the old bulk alloy, there is a mixed growth with a cationic part (external layer) and an anionic one (internal layer).

4. Discussion

4.1. Proposed corrosion mechanisms on P-type samples

Based on the results concerning the growth of the oxide layer, the dissolution and the oxide structure, a corrosion mechanism of Alloy 690 in SCW conditions is proposed for the polished state (Fig. 11) according to the following points. (i) The external oxide layer growth is cationic whereas the internal layer growth is anionic. (ii) The external oxide layer is mostly composed by nickel and iron rich oxide, probably nickel ferrite $Ni_xFe_{3-x}O_4$. (iii) The internal oxide layer is enriched in chromium and consists

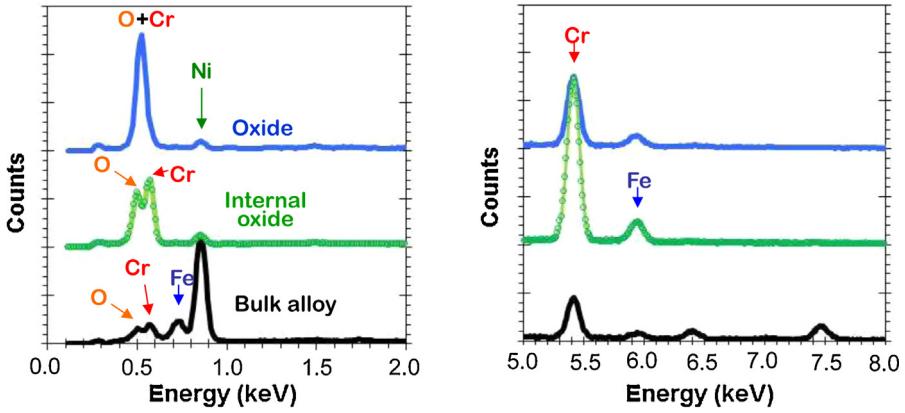

Fig. 8. EDX analyses of *M* sample oxidized 840 h in SCW conditions (600 °C, 25 MPa) in the continuous oxide layer, in the internal oxide and in the alloy bulk.

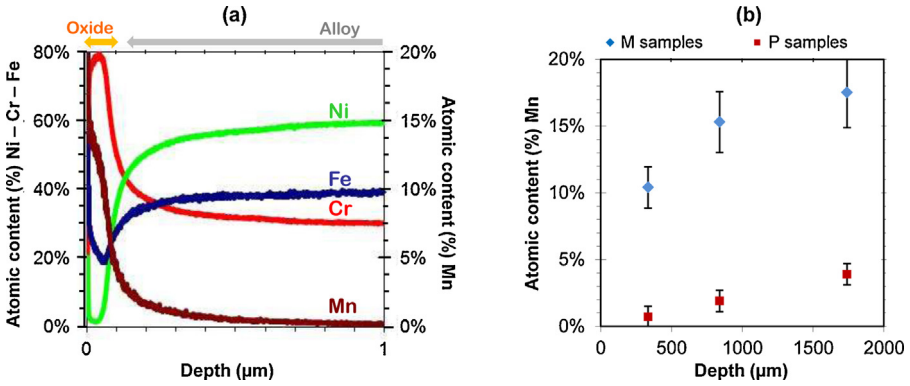

Fig. 9. Fe, Cr, Ni, and Mn GDOS atomic profiles normalized to the total metallic elements (*i.e.*, without taking oxygen into account) from *M* sample exposed 840 h in SCW (a) and Mn maximum contents in the oxide scale formed on different Alloy 690 samples oxidized in SCW (b).

Table 2
ICP-OES cations measurement after SCW corrosion tests of 335 h, 840 h, and 1740 h. Data are normalized to the whole polished surface area (3.5×10^{-3} m^2).

Exposure time (h)	Fe (µg/mL/cm^2)	Cr (µg/mL/cm^2)	Ni (µg/mL/cm^2)	Mn (µg/mL/cm^2)	Cooling time (h)
0	0[a]	0[a]	0[a]	0[a]	
335	7.4×10^{-2}	0[a]	2.7×10^{-2}	1.4×10^{-2}	20
840	0.37	0[a]	0.8	1.9×10^{-2}	20
1740	3.25	4.8×10^{-3}	0.8	0.12	40

[a] Corresponds to the limit of detection.

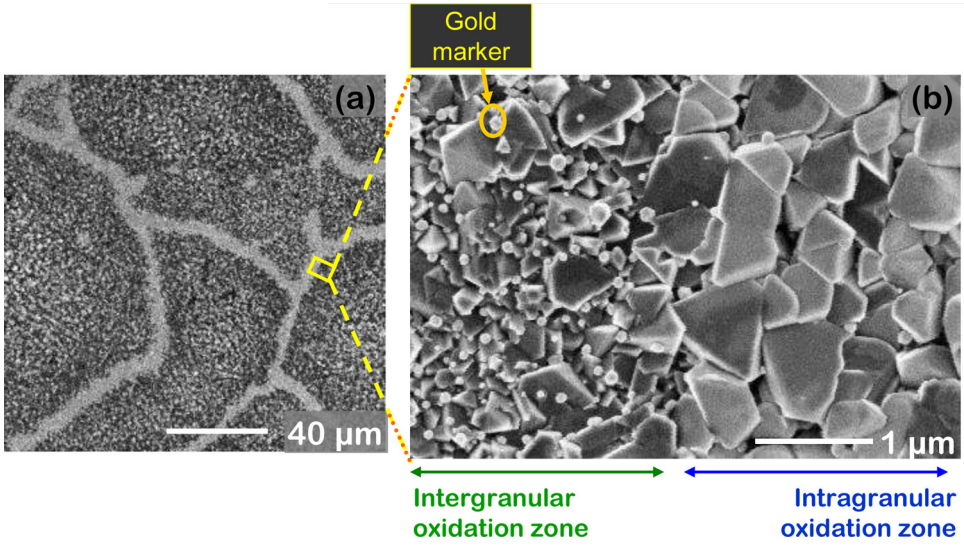

Fig. 10. SEM observations of *P* sample oxidized 335 h in SCW conditions (600 °C, 25 MPa). (a) Surface view showing the alloy microstructure revealed by oxidation [*acceleration voltage 1 kV, secondary electron image*] and (b) surface view showing gold markers on the intergranular zone whereas, gold markers are hidden by the oxide formed on the intragranular zone [*acceleration voltage 3 kV, secondary electron image*].

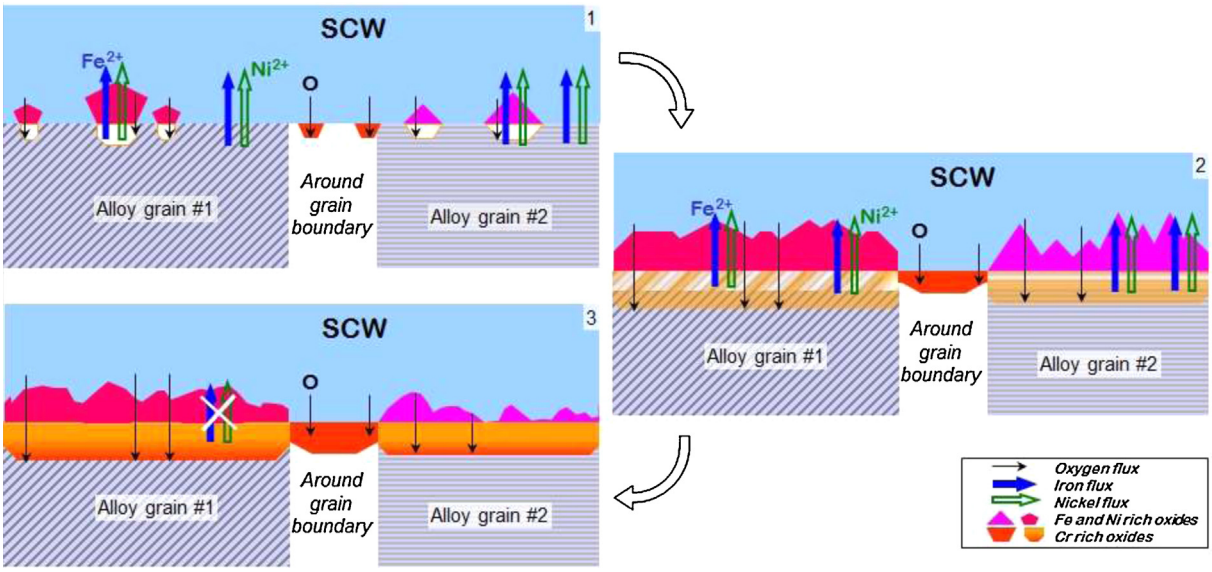

Fig. 11. Proposed sketch of corrosion mechanisms of Ni base alloys in hydrogenated supercritical water.

of α-chromia Cr_2O_3 and also mixed chromite containing manganese $(Mn,Fe,Ni)Cr_2O_4$. (iv) The oxide growth depends on alloy microstructure. Grain boundaries favor chromium rich oxide while iron and nickel rich oxide are formed above the underlying intragranular zone. (v) Nickel and iron can be released in SCW by the dissolution of external layer. As in the PWR, the release of metallic elements in the SCW environment may be problematic in the case of nuclear applications. The variations of temperature along the coolant circuits could provoke local precipitation and consequently accumulation could occur. Although it could be of interest to assess the release after the formation of the continuous chromium oxide layer.

During this corrosion process, two different zones are identified, an intragranular one and an intergranular one. There is a competition between the growth of iron and nickel rich oxide and chromium rich oxide. The alloy grain boundaries seem to be preferential zones for chromium rich oxide growth, whereas, iron and nickel rich oxide appears preferentially above intragranular zone.

Above the underlying alloy grains, cationic diffusion through the nickel and iron rich oxide feeds its growth. At the same time, the selective oxidation of iron and nickel leads to chromium enrichment. Thus, with increasing depth, the oxide becomes enriched in chromium. Indeed chromium is the most oxidizing element whereas the oxidizing strength decreases with depth due to the transport phenomenon. Consequently, on the intragranular zone, there are two oxide layers. On the top, there is a mixed spinel rich in nickel and iron. This layer would have a cationic growth. The dissolution of the metallic species in SCW is also significant and should play a role. The uppermost oxide layer could grow due to the cation flux from the metal but can also be dissolved. The results tend to show that growth rate is higher than dissolution rate up to oxidation times between 335 h and 840 h.

With time, the ratio is inverted: the dissolution rate becomes higher than the growth rate. This corresponds to the growth of the internal oxide layer. The inner chromium rich oxide becomes a diffusion barrier for cationic species, such as the oxide formed at intergranular zones. Thus, the external layer is not supplied and the nickel and iron rich spinel starts to dissolve. This is in agreement with the described dissolution of the external oxide layer of the intragranular zone. The dissolution carries on until the solubility limits were reached.

Concerning the oxide growing on grain boundaries, these act as short circuit for chromium diffusion. This lead to a chromium rich oxide (chromia or/and mixed chromite). Chromium oxide, especially α-chromia, limits the diffusion of iron and nickel [27–31]. For this reason, there is a limited cationic growth of the external oxide layer around grain boundaries. Moreover the growth is likely controlled by the diffusion through the oxide layer. Therefore, oxide growth is slow at the intergranular zone. Finally, there remains a continuous oxide layer rich in chromium whatever the oxidation zones.

4.2. *Effect of severe plastic deformation*

The surface finish of the alloy modifies the corrosion mechanism because of the induced changes in the alloy microstructure. The zone affected by severe plastic deformation leads to an ultra-fine grain microstructure from the alloy surface down to a depth of about 10 μm under the conditions studied. As *P* samples show a different behavior between intragranular and intergranular zones, it can be expected, in the case of *M* samples, that an ultra-fine grain microstructure spreads the intergranular zone behavior observed on *P* samples, to the entire surface of *M* samples. It implies that internal oxide layer growing on intragranular zone exhibits a high content of chromium (around 80%) from exposures of 335 h. In fact, the grain boundary density is also increased in comparison with *P* samples. This could improve diffusion through short circuits. An increase of the chromium supply to the oxide/alloy interface due to these diffusion paths [19] leads to chromium rich oxide, mostly composed of α-chromia.

The chromium rich oxide limits the diffusion of iron and nickel through the oxide layer [27–31]. Consequently, the external layer cannot grow. Nevertheless, an increasing content of manganese in the outer part of the internal oxide scale suggests that the oxide layer formed on *M* sample does not limit the manganese diffusion through the oxide scale. The results show that this chromium oxide layer rich in manganese strongly decreases the nickel and iron diffusion through the oxide and causes a limited external layer.

However, this oxide layer enriched in manganese is not a barrier for oxygen diffusion. Indeed, the internal oxidation shows that the oxygen diffusion occurs up to 10 μm in depth under the oxide layer. From Sarrazin et al. [32], thermodynamics for high temperature oxidation permits the internal oxidation of a binary alloy AB

according to the following conditions. (i) A is the main element of the alloy while B is added at low content. (ii) B is more sensitive to oxidation. It means that the equivalent pressure of O_2 at the oxidation equilibrium of B $P^{B}_{O_2}$ is lower than those of A $P^{A}_{O_2}$. (iii) The equivalent pressure of O_2 stands between the two equilibrium values:

$$P^{B}_{O_2} < P_{O_2} < P^{A}_{O_2}$$

In that case, B is internally oxidized in the A matrix. On the other hand, if the B content is high enough, a continuous layer of B oxide is formed on the AB alloy. Here, nickel is the main element. Chromium corresponds to the alloying element which is the most oxidizable. However, the chromium content is sufficient to form a continuous oxide layer on *P* samples. Thus, thermodynamics alone cannot explain the change in oxidation mechanism between *P* and *M* samples and kinetics interpretations would be more relevant to deal with this phenomenon.

Considering the similarity of the internal oxide layers in both cases *P* and *M*, oxygen could diffuse through the oxide scale and dissolve in the alloy at the oxide/alloy interface. The ultra-fine grain microstructure corresponds to a higher density of defects in the alloy which probably leads to a greater oxygen diffusion deeper in *M* samples. The appearance of internal oxidation could therefore be due to the numerous defects present in *M* sample compared to *P* sample. These are more nucleation sites for chromium oxide in the depth of *M* sample. These nuclei can grow thanks to the supply of oxygen and chromium through diffusion short-circuits.

5. Conclusion

The corrosion mechanisms of Alloy 690 Ni Base alloy in hydrogenated supercritical water at 600 °C and 25 MPa were investigated taking into account the surface finish and the dissolution. Oxide layers were described in terms of morphology, composition and structure.

For polished sample presenting a low defect density, the external oxide layer is composed of iron and nickel oxides. This layer grows by cationic diffusion but suffers from dissolution. The internal layer which is composed of chromium oxides grows by anionic diffusion.

For machined sample, the effect of severe plastic deformation leads to an ultrafine grain microstructure with an increase of the grain boundary density. This favors the selective oxidation of chromium and hence to a thinner chromium rich oxide. Unfortunately, the high defect density permits oxygen diffusion into the alloy resulting in internal oxidation.

Comparing to the sub-critical corrosion in liquid phase, the high temperature emphasizes the diffusion especially within the alloy grain boundaries. The high defect density introduced by milling the alloy surface leads to recrystallization and ultra-fine grains during corrosion test. The corrosion mechanism is thus dependent on the alloy grain size.

References

[1] K. Dobashi, A. Kimura, Y. Oka, S. Koshizuka, Conceptual design of a high temperature power reactor cooled and moderated by supercritical light water, Ann. Nucl. Energy 25 (1998) 487–505.

[2] J. Yoo, Y. Ishiwatari, Y. Oka, J. Liu, Conceptual design of compact supercritical water-cooled fast reactor with thermal hydraulic coupling, Ann. Nucl. Energy 33 (2006) 945–956.

[3] T.R. Allen, K. Sridharan, L. Tan, W.E. Windes, J.I. Cole, D.C. Crawford, G.S. Was, Materials challenges for generation IV nuclear energy systems, Nucl. Technol. 162 (2008) 342–357.

[4] K. Ehrlich, J. Konys, L. Heikinheimo, Materials for high performance light water reactors, J. Nucl. Mater. 327 (2004) 140–147.

[5] H. Nezakat, S. Penttilä, S. Morteza Sabet, J. Szpunar, Effect of thermo-mechanical processing on oxidation of austenitic stainless steel 316 L in supercritical water, Corros. Sci. 94 (2015) 197–206.

[6] Y. Chen, K. Sridharan, T. Allen, Corrosion behaviour of ferritic-martensitic steel T91 in supercritical water, Corros. Sci. 48 (2006) 2843–2854.

[7] L. Tan, Y. Yang, T.R. Allen, Oxidation behaviour of iron-based alloy HCM12A exposed in supercritical water, Corros. Sci. 48 (2006) 3123–3138.

[8] K.-H. Chang, S.-M. Chen, T.-K. Yeh, J.-J. Kai, Effect of dissolved oxygen content on the oxide structure of Alloy 625 in supercritical water environments at 700 °C, Corros. Sci. 81 (2014) 21–26.

[9] A.S. Kimura, M. Ukai Fujiwara, Corrosion properties of oxide dispersion strengthened steels in super-critical water environment, J. Nucl. Mater. 329–333 (2004) 387–391.

[10] A. Kimura, H.-S. Cho, N. Toda, High burnup fuel cladding materials R&D for advanced nuclear systems—nano-sized oxide dispersion strengthening steels, J. Nucl. Sci. Technol. 44 (3) (2007) 323–328.

[11] P. Ampornrat, G.S. Was, Oxidation of ferritic—martensitic alloys T91, HCM12A, and HT-9 in supercritical water, J. Nucl. Mater. 371 (2007) 1–17.

[12] L. Tan, X. Ren, K. Sridharan, T.R. Allen, Effect of shot-peening on the oxidation of alloy 800H exposed to supercritical water and cyclic oxidation, Corros. Sci. 50 (2008) 2040–2046.

[13] G.S. Was, P. Ampornrat, G. Gupta, S. Teysseyre, Corrosion and stress corrosion cracking in supercritical water, J. Nucl. Mater. 371 (2007) 176–201.

[14] W.K. Boyd, H.A. Pray, Corrosion of stainless steels in supercritical water, in: 12th Annual Conference, NACE, New York, USA, 1956.

[15] L. Tan, X. Ren, K. Sridharan, T.R. Allen, Corrosion behavior of Ni-base alloys for advanced high temperature water-cooled nuclear plants, Corros. Sci. 50 (2008) 3056–3062.

[16] D. Guzonas, J. Wills, T. Do, J. Michel, Corrosion of candidate materials for use in a supercritical water CANDU® reactor, in: 13th International Conference on Environmental Degradation of Materials in Nuclear Power Systems, Whistler, British Columbia, 2007.

[17] X. Zhong, E.-H. Han, X. Wu, Corrosion behavior of Alloy 690 in aerated supercritical water, Corros. Sci. 66 (2013) 369–379.

[18] J.E. Maslar, W.S. Hurst, W.J. Bowers Jr., J.H. Hendricks, E.S. Windsor, Alloy 600 aqueous corrosion at elevated temperatures and pressures: an in situ raman spectroscopic investigation, J. Electr. Soc. 156 (2009) 103–113.

[19] C. Ostwald, H.J. Grabke, Initial oxidation and chromium diffusion. I. Effects of surface working on 9–20% Cr steels, Corros. Sci. 46 (2004) 1113–1127.

[20] H. Lefaix-Jeuland, L. Marchetti, S. Perrin, M. Pijolat, M. Sennour, R. Molins, Oxidation kinetics and mechanisms of Ni-base alloys in pressurised water reactor primary conditions: Influence of subsurface defects, Corros. Sci. 53 (2011) 3914–3922.

[21] M. Montgomery, O.H. Larsen, S.A. Jensen, Ole biedefield investigation of steamside oxidation for TP347H, Mater. Sci. For. 461–464 (2004) 1007–1014.

[22] W. Wagner, A. Pruß, The IAPWS formulation 1995 for the thermodynamic properties of ordinary water substance for general and scientific use, J. Phys. Chem. Ref. Data 31 (2002) 387–535.

[23] P. Kritzer, Corrosion in high-temperature and supercritical water ad aqueous solutions: a review, J. Supercrit. Fluids 29 (2004) 1–29.

[24] A. Machet, A. Galtayries, S. Zanna, L. Klein, V. Maurice, P. Jolivet, M. Foucault, P. Combrade, P. Scott, P. Marcus, XPS and STM study of the growth and structure of passive films in high temperature water on a nickel-base alloy, Electrochim. Acta 49 (2004) 3957–3964.

[25] K.-H. Chang, J.-H. Huang, Corrosion behavior of Alloy 625 in supercritical water environments, Prog. Nucl. Energy 57 (2012) 20–31.

[26] M. Sennour, L. Marchetti, F. Martin, S. Perrin, R. Molins, M. Pijolat, A detailed TEM and SEM study of Ni-base alloys oxide scales formed in primary conditions of pressurized water reactor, J. Nucl. Mater. 402 (2010) 147–156.

[27] A.C.S. Sabioni, B. Lesage, A.M. Huntz, J.C. Pivin, C. Monty, Self-diffusion in Cr_2O_3. I. Chromium diffusion in single crystals, Philos. Mag. 66 (1992) 333–350.

[28] A.C.S. Sabioni, A.M. Huntz, F. Millot, C. Monty, Self-diffusion in Cr_2O_3. II. Oxygen diffusion in single crystals, Philos. Mag. 66 (1992) 351–360.

[29] A.C.S. Sabioni, A.M. Huntz, F. Millot, C. Monty, Self-diffusion in Cr_2O_3. III. Chromium and oxygen grain-boundary diffusion in polycrystals, Philos. Mag. 66 (1992) 361–374.

[30] A.C.S. Sabioni, A.M. Huntz, F. Silva, F. Jomard, Diffusion of iron in Cr_2O_3: polycristals and thin films, Mater. Sci. Eng. A 392 (2005) 254–261.

[31] R.E. Lobnig, H.P. Schmidt, K. Hennesen, H.J. Grabke, Diffusion of cations in chromia layers grown on iron-base alloys, Oxid. Met. 37 (1992) 81–93.

[32] P. Sarrazin, A. Galerie, J. Fouletier, Mechanisms of High Temperature Corrosion: A Kinetic Appoach, Trans Tech Publications, Ltd., Zurich, Switzerland, 2008.